The Impact of Spectral Band Characteristics on Unmixing of Hyperspectral Data for Monitoring Mine Tailings Site Rehabilitation

J. Lévesque[1)], K. Staenz[2)], and T. Szeredi[3)]

[1)]MIR Télédétection Inc., 2182 de la Province, Longueuil, QC, J4G 1R7, Canada
Email : josee.levesque@ccrs.nrcan.gc.ca

[2)]Canada Centre for Remote Sensing, 588 Booth St., Ottawa, ON, K1A 0Y7, Canada

[3)] MacDonald Dettwiler and Assoc., 13800 Commerce Parkway, Richmond, BC, V6V 2J3, Canada

SUMMARY

This paper demonstrates the impact of band characteristics on spectral unmixing of Compact Airborne Spectrographic Imager (*casi)* reflectance data acquired in the visible near-infrared spectral range over the Copper Cliff mine tailings site near Sudbury (Ontario, Canada). Spectral unmixing is used to monitor the rehabilitation status. For this purpose, the bands were reduced systematically from 65 to 33, 17, 8 and 4 bands using the original *casi* bandwidth of 8.7 nm full width at half maximum (FWHM). An interpolated data set using a cubic spline was derived from the 65-band *casi* spectra to study the effect of the bandwidth. The bandwidth at FWHM was varied between 8.5 nm and 76.5 nm in increments of 8.5 nm for six selected band positions across the *casi* wavelength range. High spatial resolution Ikonos 2 multispectral sensor image data with less bands and larger bandwidths than *casi* were simulated in order to investigate the combined effect of number of bands and bandwidth. These data cubes were unmixed with a constrained linear approach involving the endmembers green vegetation, lime, oxidized tailings, and two different water types. A comparison of the unmixing results indicates a mean absolute difference of up to 0.02 (standard deviation: $\pm$ 0.05) between the endmember fractions of the simulated data versus the 65-band benchmark data if the bands are selected according to physical spectral properties. The errors are much larger if the bands are not positioned properly. In general, the unmixing of the simulated data, including the four broad-band Ikonos simulation case, produced similar results as with

the full 65-band *casi* as long as the bands are positioned with respect to physical spectral properties. Such a result, especially for the broad-band simulations, was achieved mainly because the endmembers are spectrally very distinct and do not show subtle differences.

RÉSUMÉ

Cette étude démontre l'importance de la position, du nombre, et de la largeur des bandes spectrales sur les résultats de déconvolution spectrale des données de réflectance du Compact Airborne Spectrographic Imager (*casi*). Les données ont été acquises dans le visible et le proche infrarouge pour le site de rejets miniers de la mine Copper Cliff près de Sudbury (Ontario, Canada). Afin d'étudier l'effet du nombre de bandes spectrales, les données *casi* ont été réduites de façon systématique de 65 à 33, 17, 8 et 4 bandes en maintenant la largeur de bande initiale de 8,7 nm à mi-hauteur. Pour étudier l'effet de la largeur des bandes, une série de données interpolées par une fonction cubique a été créée à partir des spectres des données originales *casi* de 65 bandes. Une image de six bandes spectrales pré-sélectionnées a été produite pour chaque largeur de bande à mi-hauteur variant entre 8,5 nm et 76,5 nm avec un intervalle de 8,5 nm. Les données multispectrales à haute résolution spatiale Ikonos 2 (comportant des fenêtres spectrales plus larges et moins nombreuses que *casi*) ont été simulées afin d'étudier l'effet combiné du nombre et de la largeur de bande. Une déconvolution spectrale linéaire a été appliquée sur les données à partir de la signature spectrale de 5 composantes élémentaires : végétation, chaux, rejets miniers oxydés, et deux types de surfaces d'eau. Les résultats montrent une différence absolue moyenne allant jusqu'à 0,02 (écart-type: ± 0,05) entre les fractions des composantes élémentaires des données simulées et celles provenant de la série de données originales *casi* de 65 bandes lorsque que les bandes spectrales sont sélectionnées selon des propriétés physiques et spectrales. La différence absolue moyenne est beaucoup plus élevée lorsque les bandes sont positionnées de façon aléatoire. En général, la déconvolution spectrale des données simulées produit des résultats semblables à ceux obtenus avec la série de données originale *casi* de 65 bandes dans la mesure où la position des bandes spectrales est déterminée d'après des propriétés physiques et spectrales. De tels résultats, entre autre ceux de la simulation de bandes larges, sont

réalisables en grande partie parce que les composantes élémentaires ont des signatures spectrales très distinctes.

1. INTRODUCTION

Canadian liability for acid mine drainage is in the order of $2 billion to $5 billion depending on the technique used to dispose of and treat the acidic waste (Feasby and Jones, 1994). In the Sudbury area alone, Inco Ltd. spends an annual $5 million to reclaim property (Inco, 1998). Given these enormous costs, monitoring techniques are needed to evaluate their efficiency for reclamation of mine tailings sites, e.g., revegetation (Hossner, 1988). Recent work indicated that remote sensing, especially imaging spectrometry, has the potential to play a significant role in this area (Ferrier, 1999; Shang et al., 1999 ; Mueller et al., 1997; Farrand and Harsanyi, 1997 ; Swayze et al., 1996; Singhroy, 1996). In previous studies, Lévesque et al. (1997 and 1999) demonstrated the vegetation monitoring capability of the Compact Airborne Spectrographic Imager (*casi*) over the Copper Cliff mine tailings area near Sudbury, Ontario, Canada. If long term monitoring is required airborne surveys can become quite expensive. The question is whether one can achieve similar results using Ikonos 2 and other forthcoming high spatial resolution satellites such as Orbview3 and Quickbird (ASPRS, 1996 ; Space Imaging, 1999). Table 1 summarizes the basic instument charactersitics of these sensors. The spatial resolution of these sensors is similar to that of the *casi* data acquired over the Copper Cliff mine tailings site (2.5 m by 4.3 m). However, these sensors have fewer spectral bands and their bands are wider than those of the *casi* visible-near infra-red (VNIR) hyperspectral data sets used for this study.

This paper investigates the effect of varying bandwidth and number of bands on the ability to monitor mine tailings revegetation over a site near Sudbury using a spectral unmixing approach. In addition, the four Ikonos 2 bands and related bandwidths were simulated in order to evaluate their potential monitoring capability. Since Orbview3 and Quickbird have basically the same spectral configuration as Ikonos 2 the results obtained for Ikonos 2 are assumed to be applicable to these sensors also. The *casi* data set used for

the study presented in this paper was collected in 72 bands in 1996. The data analysis was carried out on the Imaging Spectrometer Data Analysis System (ISDAS) of the Canada Centre for Remote Sensing (Staenz et al., 1998).

2. IMAGE DATA USED

The image data was collected with a *casi* instrument in spectral mode on August 24, 1996 over the Copper Cliff mine tailings site near Sudbury, Ontario, Canada. The data set includes 72 contiguous, 8.7 nm wide, spectral bands covering a wavelength range in the VNIR from 407 nm to 944 nm (Anger et al., 1996). The instrument was flown at an altitude of 1905 m resulting in a pixel size of 2.5 m in the across track direction and 4.3 m in the along track direction. Table 2 summarizes the *casi* sensor configuration parameters. Only wavelengths between 429 nm and 913 nm (65 bands) were used from the *casi* data set because of the poor data quality of the first three bands as well as the last four bands. This is mainly due to the drop-off of the responsivity of the silicon detector at both ends of the *casi* wavelength range.

3. ANALYSIS APPROACH

Analysis of the *casi* data included removal of the most significant aircraft motion effect, surface reflectance retrieval, band simulation analysis, constrained linear spectral unmixing, and comparison of the resulting fraction images achieved with the various simulated data sets versus the one retrieved from the full *casi* data set. The data processing scheme is outlined in Figure 1.

3. 1 Pre-Processing

In order to correct for the most significant aircraft motion effect, the aircraft roll was calculated using the navigation data to calculate lateral pixel shifts for each line. These shifts were then applied to the entire image cubes on a line-by-line basis.

In the next pre-processing stage, surface reflectances were computed from calibrated (at-sensor radiance) data. The procedure applied to the data uses a five dimensional look-up table (LUT) approach with tunable breakpoints to provide additive and multiplicative coefficients for removal of scattering and absorption effects (Staenz and Williams, 1997). The LUT variables are: wavelength, pixel position, atmospheric water vapour, aerosol optical depth, and terrain elevation. This procedure has the advantage of reducing significantly the number of radiative transfer (RT) code runs thereby saving the time that would be required to run such a code on a pixel-by-pixel basis.

For the LUT generation for the different data sets, the MODTRAN3 radiative transfer code was run for the input parameters as listed in Table 3 for a low-level (5 %) and high-level flat reflectance spectrum (60%). This produces a LUT for each reflectance level. These LUTs were produced for five pixel locations equally spaced across the swath, including nadir and swath edges, and for single values of aerosol optical depth (horizontal visibility), terrain elevation, and water vapour contents. The final step involved in the LUT generation is the convolution of the model output radiances with the relative spectral response profiles of the sensor. *casi*'s response profiles were approximated by a trapezoidal-shaped line spread function.

For the retrieval of the surface reflectance, the LUTs were adjusted only for the pixel position using a bi-linear interpolation routine (Press et al., 1992) since single values for the other LUT parameters were used for the entire cube. The water vapour content was determined by applying the atmospheric correction process iteratively to sample scene spectra, while adjusting this atmospheric parameter, and selecting the value which best removed the water vapour absorption features on average. The surface reflectance of each pixel could then be computed as described in Staenz and Williams (1997). Sample reflectance spectra are displayed in Figure 2.

An assessment of the retrieved spectra revealed only minor irregularities in the reflectance data that may have originated in the sensor, or that may have resulted from

the approximations made in the atmospheric modelling and the selection of parameters. These minor band-to-band errors were not corrected.

3.2 Band Simulations

The number of bands was reduced by skipping every other band of the 65-band data cube resulting in a 33-band data set. This procedure was repeated to produce data sets containing 17, 8, and 4 bands, respectively. This systematic way to pick the bands, especially concerning the data sets with 8 and 4 bands (Table 4), is not ideal from a physical point-of-view. The bands are not properly positioned for the application focused on in this study. In order to overcome these difficulties, six *casi* bands were selected based on the spectral characteristics of vegetation for inclusion in the analysis (Staenz, 1996). This data is referred to in the paper as the geobotany data set. Band positions of this data set are listed in Table 4.

In order to test the effect of varying the bandwidth on the unmixing results, the original *casi* data were fit with a cubic spline and interpolated to a specific wavelength grid (Press et al., 1992). The grid size is determined by dividing the spectral response profile of the bands to be simulated into 20 intervals. This approach is appropriate since subtle spectral changes do not occur for the target type considered in this study. The interpolated data is assumed to be the underlying data set for the subsequent simulations. The interpolated values were then convolved to Gaussian spectral response profiles with full width at half maximum (FWHM) bandwidths, ranging from 8.5 nm to 76.5 nm in increments of 8.5 nm. The profiles were centred at the six band positions of the geobotany data set as listed in Table 4.

In order to consider a more realistic case with a few well selected broad bands, the spectral band characteristics of the four-band instrument onboard Ikonos 2 were simulated with the same technique as described in the previous paragraph from the *casi* 65-band data sets using Gaussian spectral response profiles. The centre wavelengths and

associated bandwidths are summarized in Table 4. The fourth band centred at 830 nm with a bandwidth of 140 nm FWHM could not be simulated properly with *casi* since the 65-band data set with an upper wavelength limit of 913 nm does not entirely cover the right tail of the response profile. Therefore, a narrower bandwidth of 83 nm FWHM was used to approximate the fourth Ikonos band. To ensure that our results are compatible with real Ikonos 2 data, the off nadir viewing direction should be limited to less that 15° (*casi* data set = ± 18°) when acquiring the data.

3.3 Spectral Unmixing

Constrained linear spectral unmixing was performed on all the simulated *casi* data cubes using an algorithm implemented in ISDAS (Szeredi et al., 1999 ; Boardman, 1989 and 1990). The method decomposes the image spectra $\vec{S}$ in terms of endmember spectra $\vec{S}_i$:

$$\vec{S} = \left(\sum_{i=1}^{N} f_i \vec{S}_i \right) + \vec{r}, \qquad (1)$$

where $0 \le f_i \le 1$, $\sum_{i=1}^{N} f_i = 1$ and f_i is the fraction of endmember *i* contributing to the image spectrum $\vec{S}$, N is the total number of endmembers, and $\vec{r}$ is the error term. The result of the unmixing procedure is a set of N fraction images that show the fractional abundance of the endmembers. Endmember spectra were selected from the 65-band image cube using the first three principal components (PCs) which account for 77%, 21% and 1% of the variability, respectively. Endmembers are the purest pixel spectra in the data set and are often located at the extremities of the scatter plot which results when the spectral data are plotted in PC space. Five endmembers were selected from the 65-band data as shown in Figure 3. These endmembers were identified as lime, green vegetation, oxidized tailings, water 1, and water 2 using field reference information in combination with ground-based spectral measurements collected with a GER3700 field spectroradiometer.

Water 2 is distinct from water 1 because of it's high content of sewage, tailings, and lime. The spectra of these endmembers are displayed in Figure 4. According to the PC scatter plots, the same five endmembers were identified for the different simulated data cubes. The endmembers for the different simulations were then generated from the endmembers of the 65-band data the same way as the simulated data sets discussed in the previous section.

3.4 Assessment of Results

The fraction images retrieved with the spectral unmixing procedure from the simulated data sets were then compared to those extracted from the 65-band data. The absolute values of the differences between the fractions found using the 65-band data and that found using the sub sampled multispectral data sets, were computed on a pixel-by-pixel basis for each endmember. Subsequently, the mean and standard deviation of these absolute differences were calculated.

4. RESULTS

As an example of the output of the constrained unmixing, the fraction images of vegetation, lime, and oxidized tailings retrieved from the 65-band data cube are shown in Figure 5 together with a colour composite providing an overview of the study site. The upper part of Figure 5a is the inactive tailings where most of the revegetation work is being done. Some of the typical areas of the tailings are identified in the colour composite and depicted in the adjacent photographs. The three endmembers shown are those most important for tailings rehabilitation purposes. The fractions vary between 0 and 1 with blue representing a low value and red a high value. The lower part of Figure 5a is an active tailings area where fresh tailings are being deposited.

An examination of the error images associated with spectral unmixing (Eq.1) of the 65-band data revealed no significant errors and hence, one can be confident all major endmembers have been found and the endmembers span the data space. In addition, the unmixing results have been validated in the field as reported by Staenz et al. (1999). Therefore, the fraction images derived from this data cube represent an ideal reference for this study.

4.1 Band Reduction

Figure 6 shows the effect of decreasing the number of *casi* bands on the spectral unmixing results. The mean absolute differences remain under 0.02 (standard deviation: $\pm$ 0.03) for all the endmembers using 33, 17, and 8 bands. When considering four bands the overall mean absolute difference increases but remains below 0.04 ($\pm$ 0.05) for green vegetation and lime and below 0.05 ($\pm$ 0.06) for oxidized tailings, respectively. These errors decrease to the same level as for the 33, 17, and 8 band cases when the bands are selected according to physical spectral properties as is the case for the 6-band geobotany data set. The two water endmembers consistently display a higher mean absolute difference than the other endmembers. This can be understood from Eq. 1. The water endmember spectra, $\vec{S}_{w1}$ and $\vec{S}_{w2}$, are relatively dark, hence the spectral magnitudes $\left|\vec{S}_{w1}\right|$ and $\left|\vec{S}_{w2}\right|$ are small compared to the other endmembers. Due to this fact the fractions f_{w1} and f_{w2} can vary by a relatively large amount without changing significantly the sum spectrum in Eq. 1. The constrained unmixing takes advantage of this fact and hence the fractions f_{w1} and f_{w2} vary more than the fractions of the other endmembers.

4.2 Varying Bandwidth

The comparison between the fractions retrieved from the 65-band data and the data sets of different bandwidth simulated from the geobotany image cube revealed mean absolute differences below 0.008 ($\pm$ 0.021) for the vegetation, lime, and oxidized tailings endmembers. The maximum mean absolute difference values occured at the 8.5 nm bandwidth. A similar trend was found for the endmembers water 1 and water 2 but with a higher mean absolute difference of up to 0.021 ($\pm$ 0.051). The standard deviation of the absolute difference decreases for all endmembers as the bandwidth increases since the local variations (in wavelength) in the spectrum are smoothed over. This results in less fractional variations and a smaller standard deviation. As an example, Figure 7 shows the mean and standard deviation of the absolute difference for the green vegetation and water 1 endmembers.

4.3 Ikonos Simulation

In Figure 8 the mean absolute difference is shown for each endmember for the Ikonos 2 simulation unmixing results against the 65-band unmixing results. Unlike for the four-band case used in Figure 6, the four Ikonos 2 bands display lower mean absolute differences. This was expected since the four Ikonos bands are better positioned to enhance differences between spectra. The mean absolute difference for all endmembers do not exceed 0.014 ($\pm$ 0.07). As pointed out before, the two water endmembers, followed by the oxidized tailings, the green vegetation and the lime endmembers, show an inverse relationship between their spectral reflectance magnitude and their mean absolute difference. Similarly, the standard deviation of the mean absolute difference is related to the magnitude of the endmember spectra which indicates that more variation is expected when using low reflectance endmembers such as water 1 and water 2.

As an example, the spatial representation of the Ikonos simulation analysis is presented in Figure 9 for the green vegetation endmember. Figures 9a and b depict the fractions retrieved from the 65-band and the simulated Ikonos data , respectively. The absolute difference map of these fraction images is shown in Figure 9c. The bluish portion of the difference map indicates lower differences while the red parts show higher differences. 98.8 % of the data are in the absolute difference range of 0.00 to 0.05.

5. DISCUSSION

Although the results indicate generally a reasonable agreement between the endmember fraction images retrieved from the simulated data sets versus the 65-band data, several points have to be considered.

The separation and identification of endmembers becomes more difficult if one moves from hyperspectral data towards multispectral broad-band data. The limited spectral resolution combined with a limited number of bands makes it difficult to separate spectrally subtle differences in endmember spectra and, subsequently, can be expected to lead generally to poor unmixing results. However, since the endmembers in this study are spectrally very different, the unmixing of the simulated broad-band Ikonos 2 data produced fractions similar to those resulting from unmixing of the *casi* 65-band data. This result is consistent with the results of the bandwidth simulation analysis using well-defined band positions for the application under consideration. However, the unmixing results are strongly affected if the bands are not positioned properly for a given application as shown in Figure 6 with the band reduction analysis.

The endmembers for a specific simulated data set were computed the same way as the image data set itself, e.g., for the Ikonos simulation the endmember spectra of the 65-band data were convolved to the Ikonos four-band characteristics. In order to evaluate the impact of this approach on the fraction images, the endmembers were also extracted from the simulated data sets themselves. The latter procedure is usually the preferred approach since scaling issues between image data and endmembers of ground (library) spectra can be avoided. However, if spectra from a library are used as endmembers, then the band characteristics of the sensor under consideration have to be simulated from those spectra. No significant differences were found between fractions retrieved with endmembers selected from the simulated data sets directly and via the 65-band data.

The unmixing procedure requires N–1 bands to unmix N endmembers. With five endmembers retrieved from the data sets under consideration, the number of bands was limited to four in this study. Complicated scenes containing more endmembers might need more bands to perform unmixing than provided by the forthcoming high spatial resolution sensors such as onboard Ikonos 2. Accordingly, the unmixing procedure cannot be applied in such cases using this type of sensor. Other methods such as traditional classification approaches (e.g. maximum likelihood) could be used, but they are not able to provide the same detailed target information as spectral unmixing.

6. CONCLUSIONS

The influence of spectral band characteristics (number of bands, bandwidth) on spectral unmixing have been investigated for monitoring the rehabilitation status of mine tailings. For this purpose, different band sets, including the four-band multispectral sensor onboard Ikonos 2, have been simulated from hyperspectral VNIR 65-band *casi* surface reflectance data. The resulting endmember fractions for green vegetation, lime, oxidized tailings, water 1, and water 2, retrieved from the simulated data sets, have been compared against those obtained from the 65-band data.

The unmixing results obtained for the different endmembers by decreasing the number of bands produces mean absolute differences that do not exceed 0.02 (standard deviation: ± 0.03) for 33-band, 17-band and 8-band data sets. The 4-band data set yields larger differences, up to 0.14 (± 0.22). However, Ikonos 2 simulation indicates that a mean absolute difference of 0.014 is achievable if the bands are selected according to physical spectral properties. The largest mean absolute differences between the fraction images occur for water 1 and water 2. This is also true for the bandwidth simulation study. It revealed mean absolute differences of a magnitude similar to those resulting from the band reduction study with the exception of the 4-band simulation. In this case, the mean absolute difference is significantly lower for the bandwidth cases, about 7 to 10 times depending on the endmember. Furthermore, the bandwidth simulation results indicate that as bandwidth increases, the standard deviation of the mean absolute difference decreases.

The study shows that especially for the non-water endmembers, which are most important for revegetation monitoring, similar unmixing results were obtained using the simulated data as retrieved with *casi* hyperspectral data as long as the bands are positioned according to physical spectral properties. This is even true for the four broad-band Ikonos 2 simulation. However, for sensors with similar band characteristics as Ikonos 2, the results cannot be readily transferred to more complicated scenes and hence, containing more endmembers than the scene used in this study. This is due to the required minimum number of bands, N-1, for unmixing N endmembers. It is also more difficult to identify endmembers, especially when subtle differences occur, if only a few spectral bands are available. Nevertheless, the study demonstrated that high spatial broad-band sensors such as Ikonos 2 and Quickbird have the potential for monitoring mine tailings rehabilitation using spectral unmixing.

7. ACKNOWLEDGEMENTS

The authors thank The Centre for Research in Earth and Space Technology (CRESTech) for the acquisition of the *casi* data and related technical support. The support of the 1996 field campaign by R. McGregor (Atomic Energy of Canada Ltd.) and A. Dumouchel (Canada Centre for Remote Sensing) and the technical assistance of J. Lefebvre (MacDonald Dettwiler and Associated) is gratefully acknowledged. Our thanks to P. Yearwood of Inco Limited for providing access to the mine tailings site and for logistical support.

8. REFERENCES

Anger, C.D., S. Achal, T. Ivanco, S. Mah, R. Price, and J. Busler, 1996, "Extended Operational Capabilities of *casi*", Proceedings of the 2nd International Airborne Remote Sensing Conference, San Francisco, California, pp.124-133.

ASPRS, 1996, "Land Satellite Information in the Next Decade – The World Under a Microscope", Executive Summary, American Society for Photogrammetry and Remote Sensing, Bethesda, Maryland, U.S.A., 72 pages.

Boardman, J.W., 1989, "Inversion of Imaging Spectrometry Data Using Singular Value Decomposition", Proceedings of the 1989 International Geoscience and Remote Sensing Symposium (IGARSS '89) and the 12th Canadian Symposium on Remote Sensing, Vancouver, British Columbia, Canada, Vol. 4, pp. 2069-2072.

Boardman, J.W., 1990, “Inversion of High Spectral Resolution Data”, Proceedings of SPIE Conference on Imaging Spectrometry of the Terrestrial Environment, Orlando, Florida, U.S.A., Vol. 1298, pp. 222-233.

Boardman, J.W., and J.F. Huntington, 1996, “Mineral Mapping with 1995 AVIRIS Data”, Summaries of the Sixth Annual JPL Airborne Earth Science Workshop, JPL Publication 96-4, Vol. 1, Pasadena, California, U.S.A., pp. 9-11.

Farrand, W.H., and C. Harsanyi, 1997, “Mapping of Mine Tailings in the Coeur d’Alene River Valley, Idaho, Through the Use of Constrained Energy Minimization Technique”, Remote Sensing of Environment, Vol. 59, pp. 64-76.

Feasby, G., and R.K. Jones, 1994, “Report of Results of a Workshop on Mine Reclamation”, Canada Centre for Mineral and Energy Technology, 18 pages.

Ferrier, G., 1999, “Application of Imaging Spectrometer Data in Identifying Environmental Pollution Caused by Mining at Rodaquilar, Spain”, Remote Sensing of Environment, 68:125-137.

Hossner, L.R., 1988, “Reclamation of Surface-Mined Lands”, CRC Press Inc., Boca Raton, Florida, U.S.A., Vol. 1, 189 pages.

Lévesque, J., Szeredi, T., Staenz, K., Singhroy, V., and Bolton, D., 1997, “Spectral Unmixing for Monitoring Mine Tailings Site Rehabilitation, Copper Cliff Mine, Sudbury, Ontario”, Proceedings of the Twelfth International Conference and Workshops on Applied Geological Remote Sensing, Denver, Colorado, U.S.A., Vol. 1, pp.340-347.

Lévesque, J., K. Staenz, J. Shang, R.A. Neville, P. Yearwood, and V. Singhroy, 1999, “Temporal Monitoring of Mine Tailings Revegetation Using Hyperspectral Data,

Sudbury, Ontario", Proceedings of the Thirteenth International Conference on Applied Geologic Remote Sensing, Vancouver, British Columbia, Canada, Vol. 2, pp. 21-28.

Inco, 1998: http://www.incoltd.com/invest/annrpt/96-env1g.htm.

Mueller, A., P. Strobl, F. Lehmann, and G. Reinhaeckel, 1997, "Case Studies of Airborne Remote Sensing for the Assessment of Mining Impacts", Proceedings of the Third International Airborne Remote Sensing Conference and Exhibition, Copenhagen, Denmark, pp. I-257-226.

Press, W.H., S.A. Teukolsky, W.T. Vetterling, and B.P. Flannery, 1992, Numerical Recipes in C, Cambridge University Press, Cambridge, England, 994 pages.

Shang, J., J. Lévesque, P.J. Howarth, B. Morris, K. Staenz, and P. Yearwood, 1999, "Preliminary Investigation of Acid Mine Drainage Detection Using *casi* Data, Copper Cliff, Ontario, Canada", Proceedings of the Fourth International Airborne Remote Sensing Conference and the 21st Canadian Symposium on Remote Sensing, Ottawa, Ontario, Canada, pp. I-771-778.

Singhroy, V.H., 1996, "Environmental and Geological Site Characterization in Vegetated Areas: Image Enhancement Guidelines", Remote Sensing and GIS for Site Characterization: Applications and Standards, eds. V.H. Singhroy, D.P. Nebert, and A.I. Johnson, ASTM STP 1279, West Coushocken, Pennsylvania, U.S.A., pp. 5-16.

Space Imaging, 1999: http://www.spaceimaging.com.

Staenz, K., 1996, "Classification of a Hyperspectral Agricultural Data Set using Band Moments for Reduction of the Spectral Dimensionality", Canadian Journal of Remote Sensing, 22(3): 248-257.

Staenz, K., and D.J. Williams, 1997, “Retrieval of Surface Reflectance from Hyperspectral Data Using a Look-Up Table Approach”, Canadian Journal of Remote Sensing, 23(4): 354-368.

Staenz, K., T. Szeredi, and J. Schwarz, 1998, “ISDAS – A System for Processing/Analyzing Hyperspectral Data”, Canadian Journal of Remote Sensing, 24(2): 99-113.

Staenz, K., Neville, R.A., Lévesque, J., Szeredi, T., Singhroy, V., Borstad, G.A., and Hauff, P., 1999, “Evaluation of *casi* and SFSI Hyperspectral Data for Geological Applications - Two Case Studies”, Canadian Journal of Remote Sensing (in press).

Swayze, G.A., R.N. Clark, R.M. Pearson, and E. Livo, 1996, “Mapping Acid-Generating Minerals at the California Gulch Superfund Site in Leadville, Colorado using Imaging Spectroscopy”, Summaries of the Sixth Annual JPL Airborne Earth Science Workshop, JPL Publication 96-4, Pasadena, California, U.S.A., Vol.1, pp. 231-234,

Szeredi, T., Staenz, K., and Neville, R.A., 1999, “Automated Endmember Selection: Part I Theory”, Remote Sensing of Environment (submitted).

Table 1 : Spectral band configuration and spatial resolution for the Quickbird, Orbview3 and Ikonos sensors.

Sensor	**Ikonos2**	**Quickbird**	**Orbview3**
Company	Space Imaging	Earthwatch	Orbital Sciences
Spectral bands (nm)	450 - 520 520 - 600 630 - 690 760 - 900	450 - 520 520 - 600 630 - 690 760 - 890	450 - 520 520 - 600 625 - 695 760 - 900
Spatial resolution	4 m	4 m	4 m

*) as of September 1999

Table 2: *casi* sensor configurations.

Spectral coverage	407-944 nm
Number of bands	72
Spectral sampling interval	7.6 nm
Bandwidth at FWHM*	8.7 nm
Sensor altitude above ground	1905 m
Ground resolution: across track along track	2.5 m 4.3 m
Swath	406 pixels

*) FWHM: Full Width at Half Maximum

Table 3: Input parameters for MODTRAN3 code runs.

Atmospheric model	Mid-latitude Summer
Aerosol model	Continental
Date of overflight	August 24, 1996
Solar zenith angle	31.5º
Solar azimuth angle	176º
Sensor zenith angle	variable
Sensor azimuth angle	variable
Terrain elevation	0.3 km
Sensor altitude above sea level	2.21 km
Water vapour content	2.35 g/cm^2
Ozone column	as per model
CO_2 mixing ratio	as per model
Horizontal visibility	50 km

Table 4: Spectral characteristics of the simulated data sets.

Data Set	**Centre Wavelength (nm)**	**Bandwidth (nm) at FWHM**
8-band	458.7, 518.2, 578.2, 638.6, 699.3, 760.28, 821.4, 882.7	8.7
4-band	503.2, 608.3, 714.5, 821.4	8.7
Geobotany (6 bands)	480.9, 548.1, 608.3, 676.5, 745.0, 829.1	8.5 to 76.5 in increments of 8.5
Ikonos 2	485, 560, 660, 830	80, 80, 60, 140

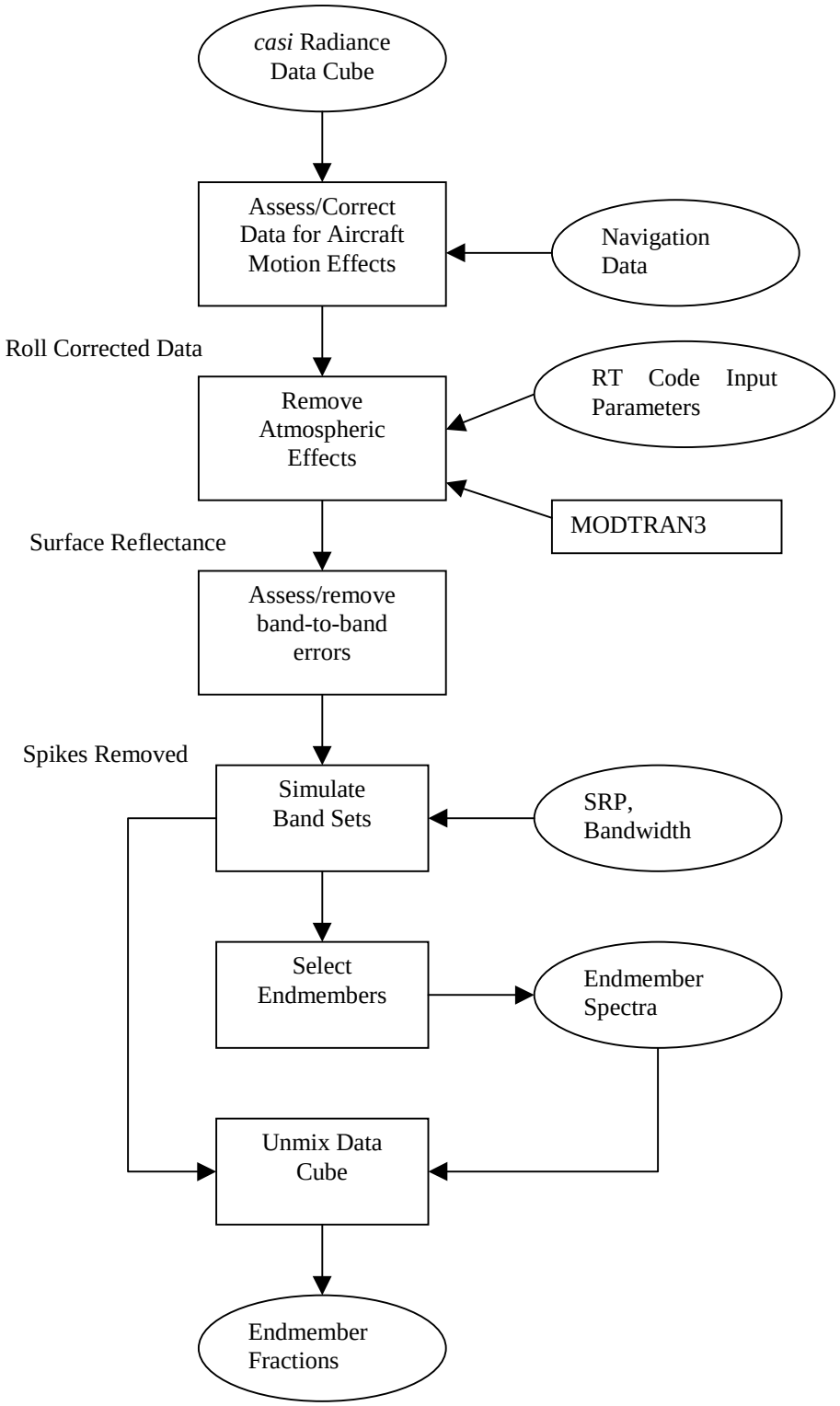

Figure 1: Data processing scheme (SRP = Spectral Response Profile).

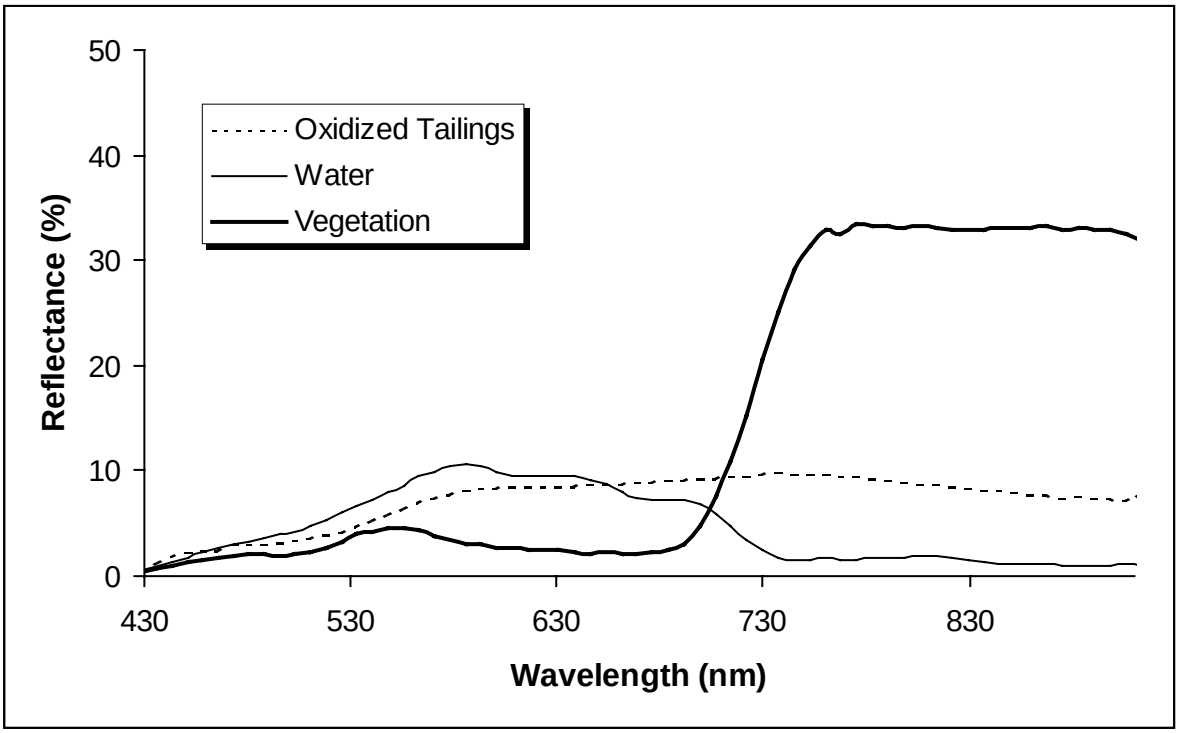

Figure 2: *casi* surface reflectance spectra retrieved from single pixels.

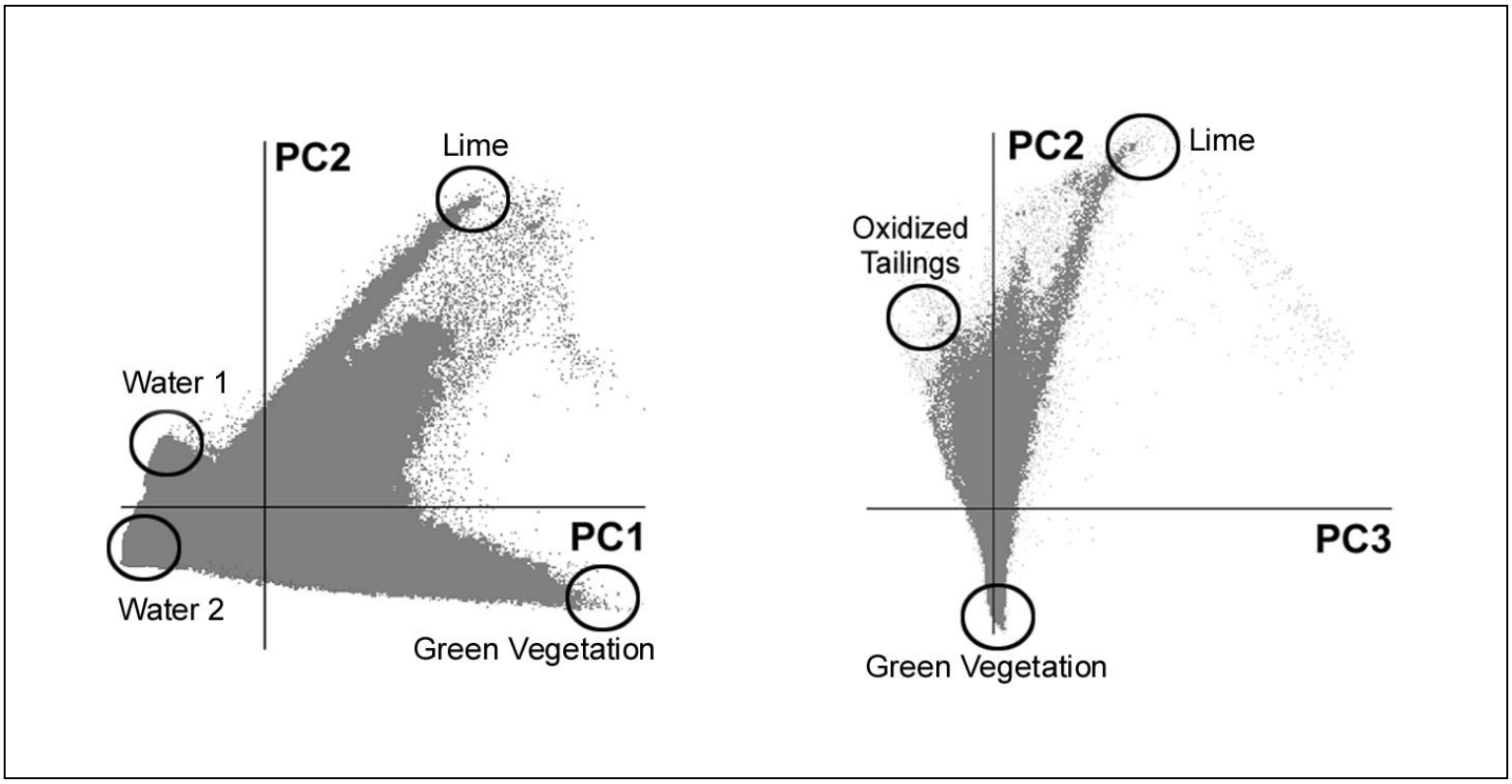

Figure 3: Scatter plots of principal component (PC) 1 versus PC2 and PC3 versus PC2 of the *casi* 65-band data.

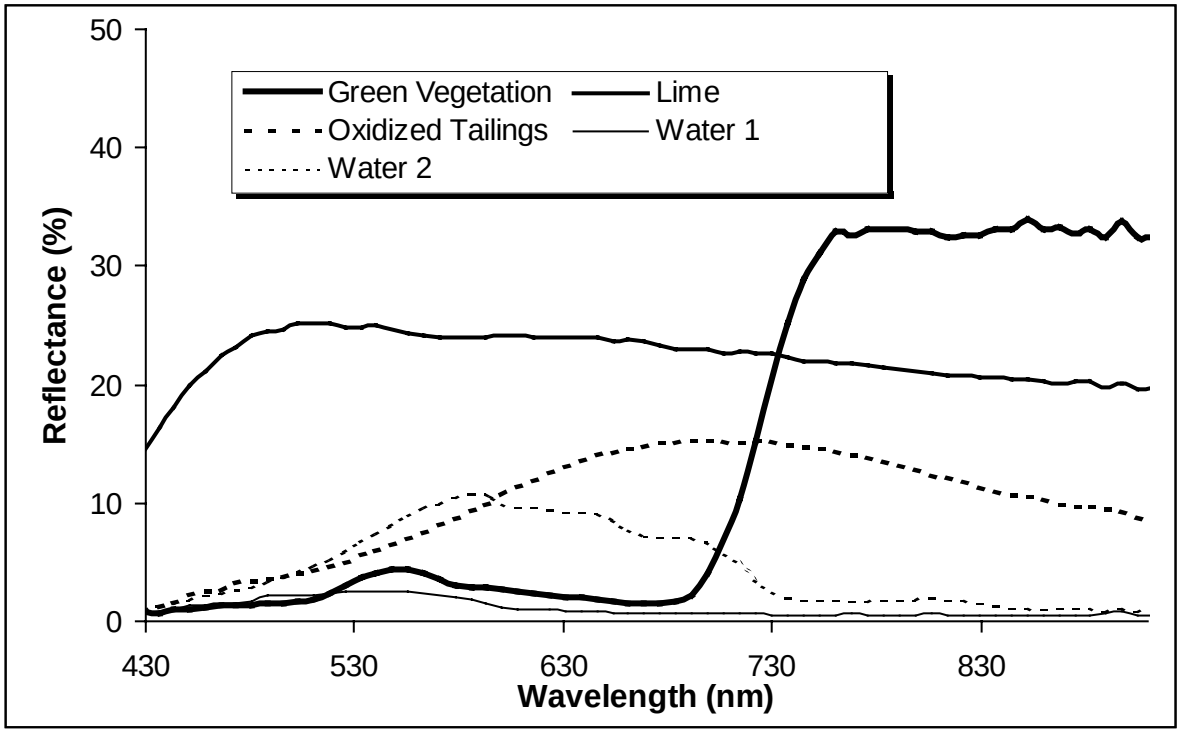

Figure 4: Endmember spectra retrieved from the 65-band *casi* data set.

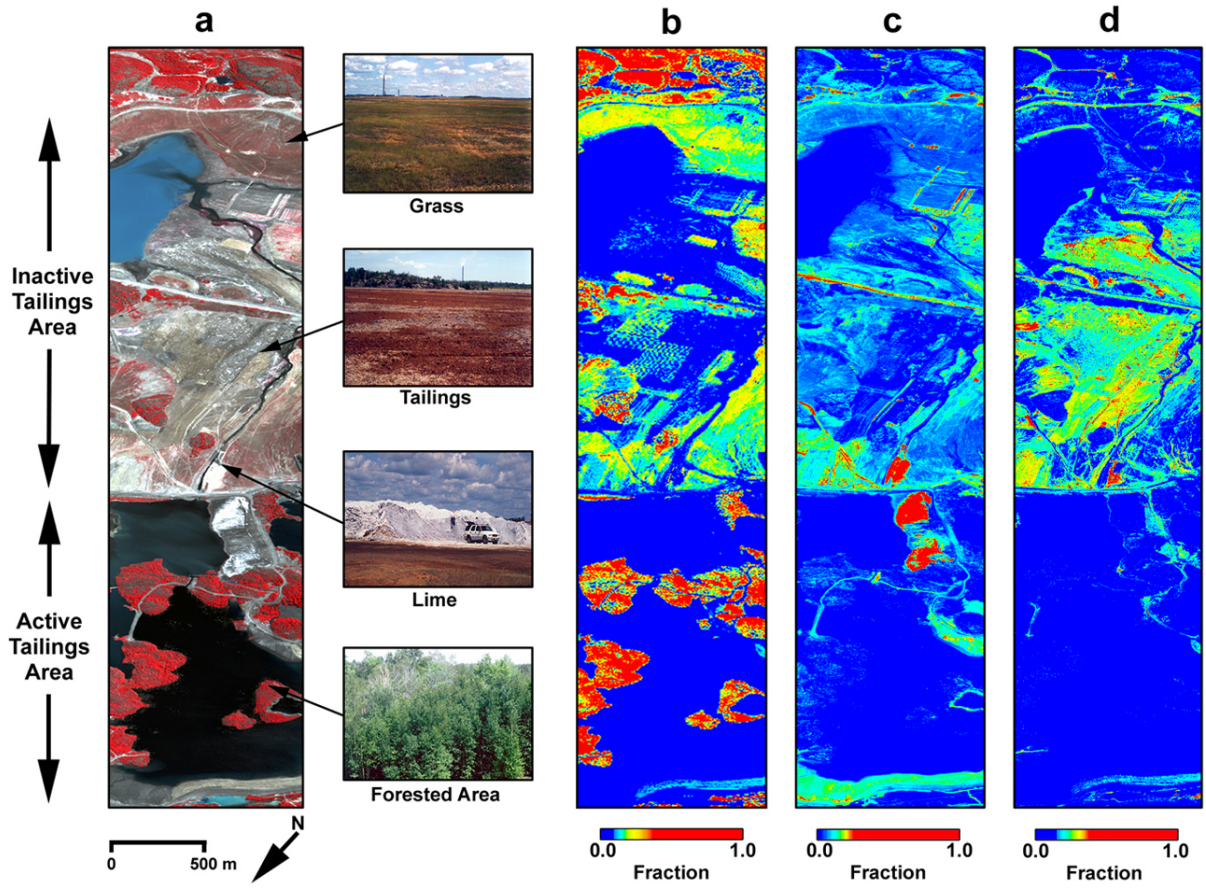

Figure 5: Colour composite and associated pictures showing (a) an overview of the tailings area with fraction images of the three endmembers (b) green vegetation, (c) lime, and (d) oxidized tailings. The colour composite retrieved from the *casi* 65-band data set was generated with bands 19 (540 nm) in the blue, 37 (676 nm) in the green, and 45 (737 nm) in the red, respectively.

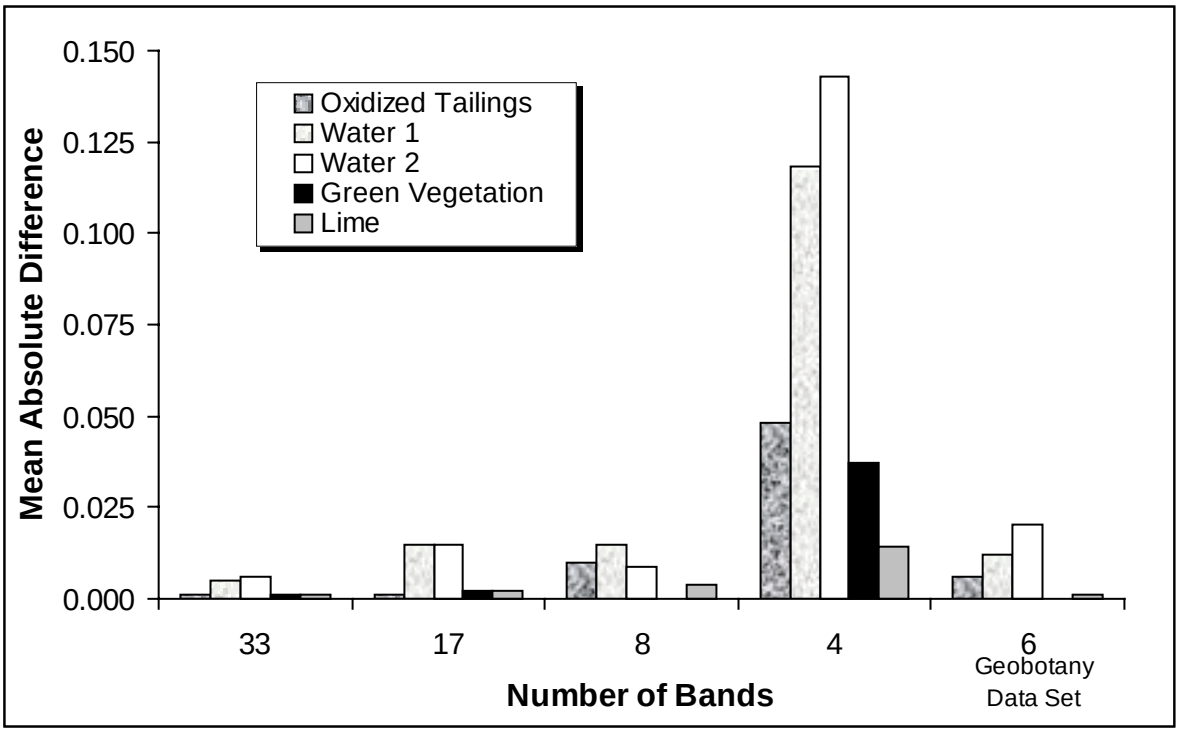

Figure 6: Mean absolute difference between the 65-band unmixing results (endmember fractions) and unmixing results of the band reduction analysis.

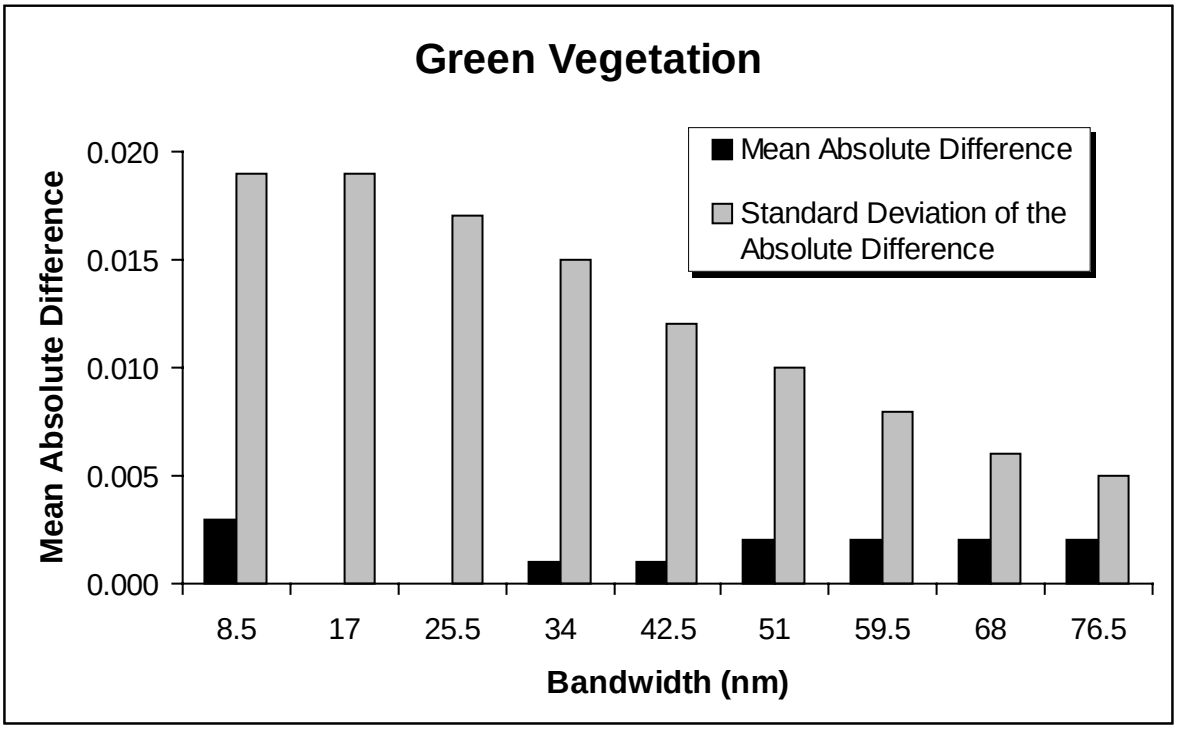

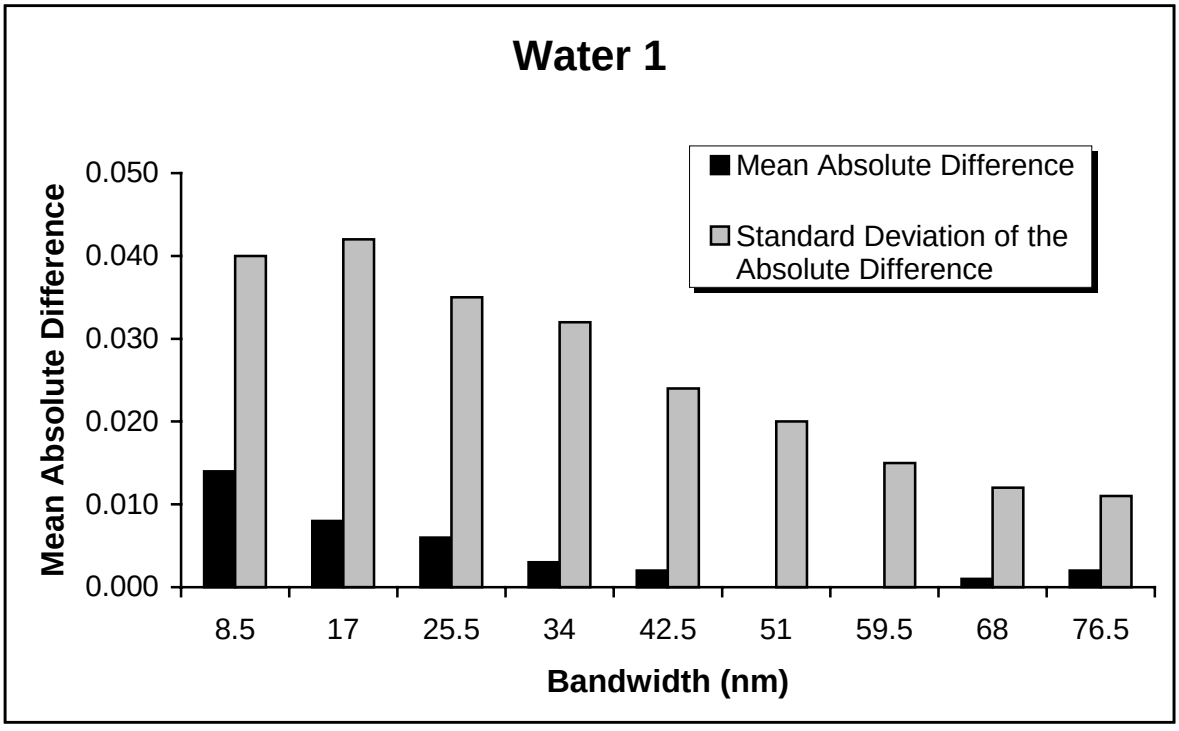

Figure 7: Mean and standard deviation of the absolute difference of the green vegetation and water 1 endmember fractions derived from the 65-band *casi* data and the different bandwidth simulations using the geobotany (6-band) data cube.

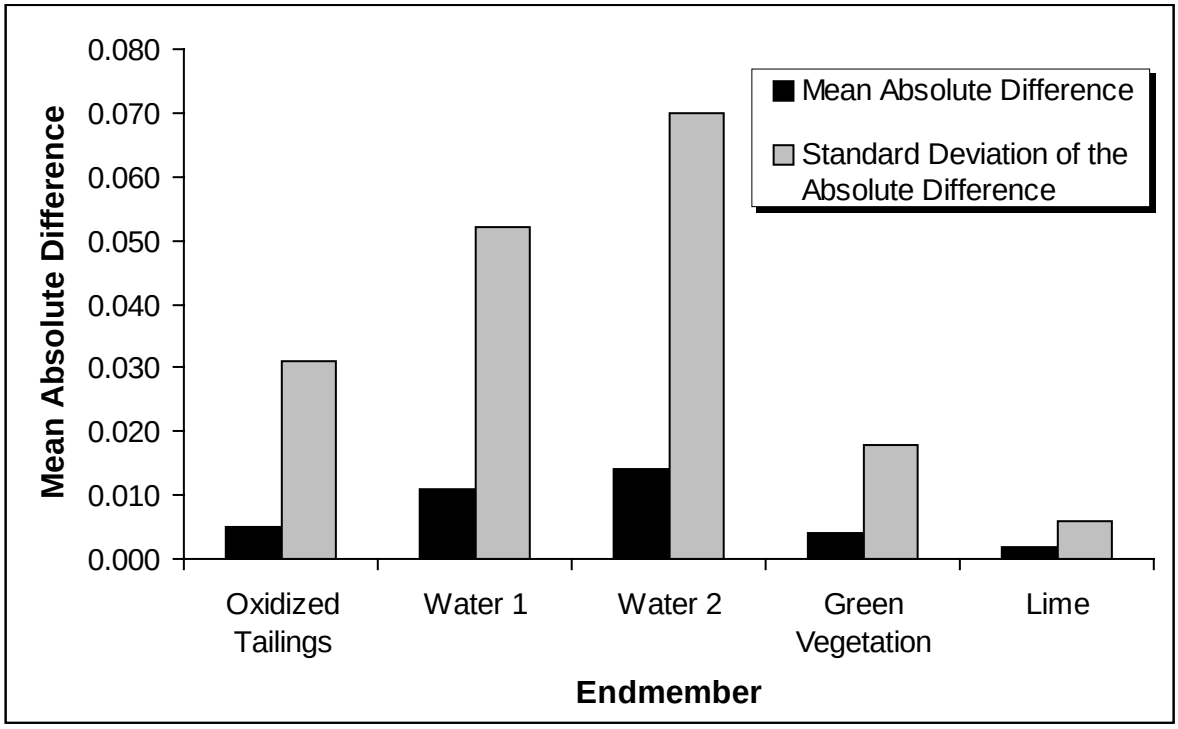

Figure 8: Mean absolute difference between the 65-band unmixing results and the Ikonos 2 simulation unmixing results for each endmember.

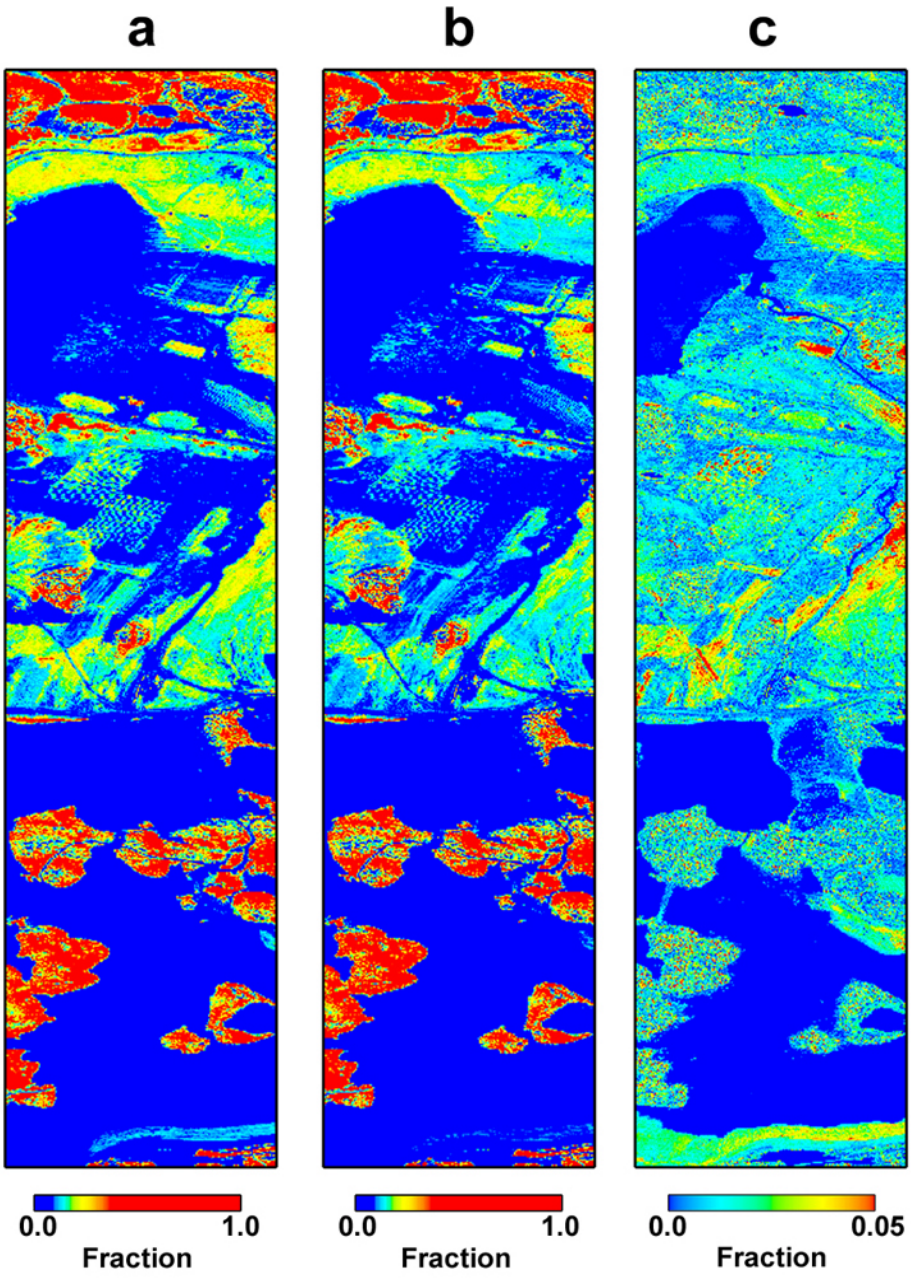

Figure 9: Fraction images retrieved from (a) the 65-band *casi* data and (b) the simulated Ikonos 2 data with (c) associated absolute difference image over the Copper Cliff mine tailings area in Sudbury.